Journal of Materials Chemistry A

MXene/graphitic carbon nitride-supported metal selenide for all-solid-state flexible supercapacitor and oxygen evolution reaction

Journal:	*Journal of Materials Chemistry A*
Manuscript ID	TA-ART-12-2024-008907.R1
Article Type:	Paper
Date Submitted by the Author:	06-Feb-2025
Complete List of Authors:	De, Shrabani; North Carolina A&T State University, Chemistry Florentino, Jose; Fayetteville State University, Chemistry and Physics Pathiraja, Gayani; North Carolina A&T State University, Chemistry Gautam, Bhoj; Fayetteville State University, Chemistry and Physics Bastakoti, Bishnu; North Carolina A&T State University, Chemistry

MXene/graphitic carbon nitride-supported metal selenide for all-solid-state flexible supercapacitor and oxygen evolution reaction

Shrabani De[a], Jose Florentino[b], Gayani Pathiraja[c], Bhoj Raj Gautam[b], Bishnu Prasad Bastakoti[a*]

[a]Department of Chemistry, North Carolina A&T State University, 1601 E. Market St. Greensboro, NC 27411 (USA)

[b]Department of Chemistry, Physics, and Materials Science, Fayetteville State University, 1200 Murchison Road, Fayetteville, NC 28301 (USA)

[c]Department of Nanoscience, Joint School of Nanoscience and Nanoengineering, University of North Carolina at Greensboro, 2907 East Gate City Blvd, Greensboro, NC 27401 (USA)

*Email: bpbastakoti@ncat.edu

Abstract

We report a new type of combination of rare earth metal selenides (Ce_2Se_3 and Er_2Se_3) with a $Ti_3C_2T_x$/S-doped graphitic carbon nitride heterostructure for bifunctional application in flexible supercapacitors and oxygen evolution reactions. The incorporation of S-doped graphitic carbon nitride in MXenes reduced the layer stacking tendency of both two-dimensional sheets and eliminated volume expansion by forming a heterostructure. Cerium and erbium rare earth metal centers induce reactive surface sites, whereas binary layers of $Ti_3C_2T_x$/S-doped graphitic carbon nitride provide a conducting matrix for the homogeneous growth of the metal selenides. The assembled all-solid-state flexible asymmetric supercapacitor exhibited a high specific capacitance of 60 F g^{-1}, an energy density of 10.1 Wh kg^{-1} (volumetric energy density: 0.9 mWh cm^{-3}) at 2 A g^{-1}, and 100% capacitance retention after 10,000 charge–discharge cycles with good flexibility for real-time applications. Furthermore, the optimum nanohybrid showed a low overpotential of 280 mV and a Tafel slope of 99 mV dec^{-1} with durable electrocatalytic performance. This work is the first to investigate the bifunctional energy efficiency of rare earth metal selenides grown over MXene materials.

Keywords: $Ti_3C_2T_x$, S-doped graphitic carbon nitride, metal selenides, all-solid-state flexible asymmetric supercapacitor, oxygen evolution reaction

1. Introduction

To address the ever-increasing energy demand and depletion of environmental resources, the exploration of inexpensive, eco-friendly, and abundant energy storage and conversion materials plays a consequential role[1, 2]. As renewable and green energy resources that consider environmental sustainability, supercapacitors, batteries, electrocatalysts, and photocatalysts have been developed significantly[3-5]. Recently, portable and wearable electronic devices have attracted increasing interest, leading to extensive studies on flexible supercapacitors. In this respect, conventional rigid supercapacitors are not capable of supplying energy for flexible electronic devices. Therefore, evolving flexible supercapacitors with efficient electrochemical characteristics is necessary to fulfill the energy demand of portable and wearable devices[6]. Generally, the electrochemical performance of energy storage and conversion devices greatly depends on the characteristics of the electrode materials. However, the performance of supercapacitors is restricted mainly by their low energy density, whereas the sluggish kinetics of the oxygen evolution reaction (OER), which is the anodic half-cell reaction of water electrolysis, is the fundamental limitation for electrocatalytic water splitting[7]. Commonly, noble metals such as Ru, Pt, Pd, and Ir-based materials have shown the best performance as electrocatalysts for the OER, but their high cost restricts their wide application[8]. On the other hand, commonly used carbonaceous electrode materials for supercapacitors are associated with low energy[9]. Therefore, investigating efficient electrode materials is crucial for developing high-performance supercapacitors as well as OER electrocatalysts.

Recently, MXenes have gained increasing attention as emerging new two-dimensional (2D) layered materials consisting of transition metal carbides, nitrides or carbonitrides due to their unique physicochemical properties[10]. Among the different transition metal-based MXenes, $Ti_3C_2T_x$ has become the most popular material in the energy field because of its excellent electrical conductivity, hydrophilicity, large volumetric capacitance, high surface area, and mechanical stability[11, 12]. However, pristine nanosheets of $Ti_3C_2T_x$ generally suffer from inevitable self-retacking, resulting in a low active surface area for the electrolyte ions and degradation of the electrochemical efficiency[13]. The incorporation of interlayer spacers can prevent the restacking tendency of MXene sheets, leading to full utilization of their active surface. Combining 2D sheet-like materials such as reduced graphene oxide (rGO), boron nitride, layered double hydroxide, or graphitic carbon nitride (g-C_3N_4) with MXenes can form heterostructure arrangements, which restricts their layer stacking and enhances their electrochemical performance[1]. The graphene analog 2D g-C_3N_4 has versatile characteristics,

such as a large surface area, tunable electrochemical properties, and stability, and the triangular nanopores of triazine and tri-s-triazine of g-C_3N_4 facilitate easy doping, defect engineering, and high edge site exposure[14, 15]. He *et al*. reported that a combination of MXene, g-C_3N_4, and rGO can be used as an efficient, stable electrocatalyst with a low onset potential of 38 mV and a Tafel slope of 76 mV dec^{-1}[16]. Additionally, Depijan *et al*. reported an increase in ion accessibility and gravimetric capacitance via the incorporation of g-C_3N_4 into $Ti_3C_2T_x$ layers[17]. Furthermore, S-doped graphitic carbon nitride has attracted more attention than their undoped versions because of the presence of nitrogen and sulfur vacancies, which enhance the electron donor-acceptor capability by offering abundant anchoring sites[18]. Despite having high stability and energy density, 2D materials are associated with low energy density, and the incorporation of redox-active centers into the electrode introduces pseudocapacitance to the system, which leads to increased energy density. Similarly, materials with redox-active centers also facilitate electrocatalytic OER performance[7, 19-21].

In this context, transition metal chalcogenides, especially selenides, have been studied as efficient electrocatalysts for the OER as well as pseudocapacitive electrodes for supercapacitors because of their high theoretical capacitance, high conductivity (~10^{-3} S m^{-1}), high charge transfer capability, stability, and low cost[22]. Owing to their interesting features, such as good electrical conductivity, high theoretical capacitance, and potential pseudocapacitive properties, earth-abundant environmentally friendly rare earth metal selenides are emerging as promising electrode materials. In this context, cerium selenide has been considered advantageous for energy storage and conversion applications. The reversible redox state ($Ce^{3+} \leftrightarrow Ce^{4+}$) can heavily contribute to pseudocapacitance in the system, which is associated with high energy density as well as interactions with oxygen ions via its adjustable interface, leading to high OER capability[23, 24]. Manzoor *et al*. reported the excellent electrocatalytic OER performance of $CeSe_2$ combined with carbon nanospheres with a 289 mV overpotential in 1 M KOH[24]. Additionally, a flexible all-solid-state supercapacitor fabricated from $CeSe_2$ delivered good specific capacitance (48.8 F g^{-1}) and energy density (11.63 W h kg^{-1})[23]. Another stable rate earth element, erbium (Er), is generally used as a dopant in transition metal selenides to increase their workability by tuning their band gap[25, 26]. However, erbium selenides (Er_2Se_3) are still not studied as electrode materials for supercapacitors or the OER. Additionally, previous studies exhibited that the incorporation of rare earth metals like Nd, Tb, Eu, and Gd can enhance the physicochemical properties of MXene by tuning their band gap energy[27-30]. Tahir et al. reported that when Gd^{3+}-doped vanadium oxide was combined with MXene the composite exhibited enhanced supercapacitor performance with specific

capacitance of 1024 F g^{-1} at 10 mV s^{-1}[31]. Still, rare earth metal combined with MXene is not explored for two electrode supercapacitor devices and OER electrocatalyst.

Inspired by the tunability and great potential of composite materials in electrochemical applications, in this study, we designed an approach to develop bifunctional electrodes consisting of rare earth metal (Ce and Er) selenide-grown $Ti_3C_2T_x$/S-doped g-C_3N_4 ternary nanohybrids via a simple hydrothermal method and tested their electrochemical efficiency as positive electrodes for all-solid-state flexible asymmetric supercapacitors as well as electrocatalysts for the OER. The electronic properties of g-C_3N_4 are tuned by S-doping and 2D/2D heterostructure formation between the MXene and S-doped g-C_3N_4 (S-CN), which restricts the layer stacking of both 2D materials and reduces the volume expansion during continuous charge–discharge. The incorporation of multiple metal centers, Ce(III) and Er(III), within the MXene/S-CN binary system (MCN) facilitates electron transfer and triggers the electrocatalytic performance of the electrode toward the OER. The heterojunctions generated within the metal selenides and binary 2D system facilitate electron transport, enhancing electrochemical performance. This combination of rate earth metal selenide with an MCN binary system has not been synthesized and studied for energy applications to date; thus, this work provides a future strategy for the development of bifunctional electrode materials for supercapacitors and the OER.

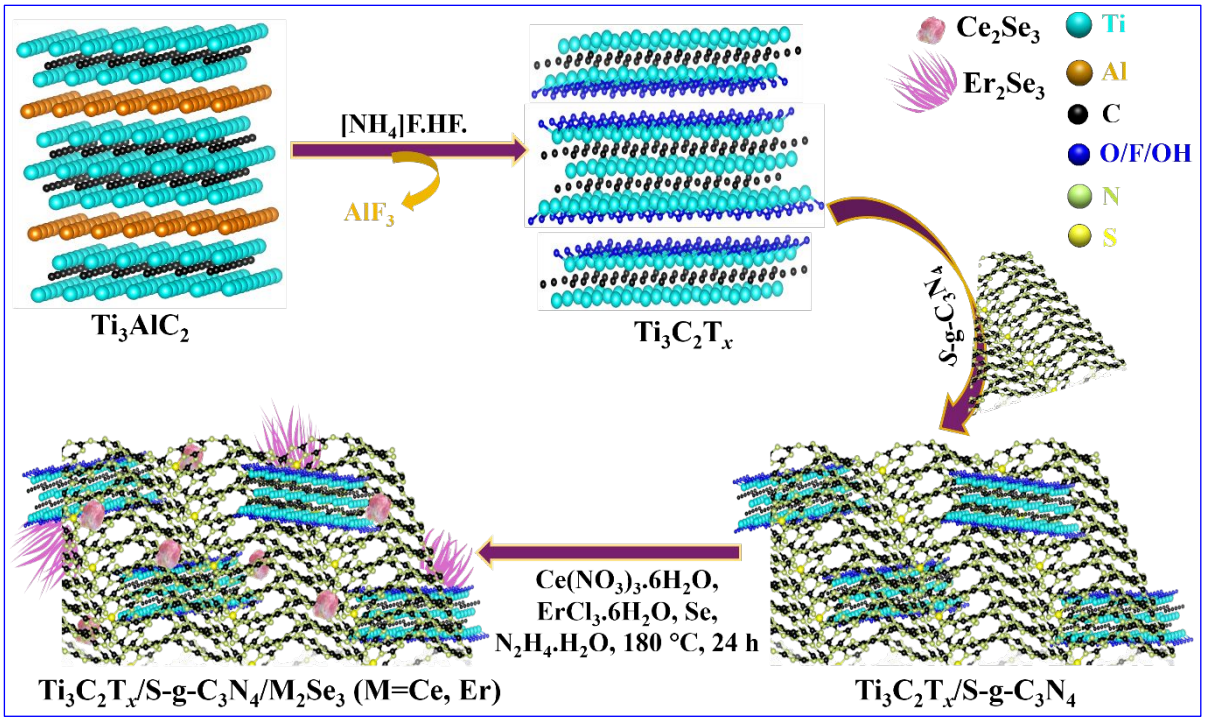

Fig. 1. Synthesis of rare earth metal selenides (Ce_2Se_3 and Er_2Se_3) with a $Ti_3C_2T_x$/S-doped graphitic carbon nitride heterostructure.

2. Results and Discussion

2.1. Optimization of MCN Binary Composites

The stepwise synthesis route for different samples is schematically illustrated in Fig. 1. The morphology of the synthesized materials was investigated via FESEM analysis. Exfoliated 2D $Ti_3C_2T_x$ sheets can be clearly visible from the FESEM images shown in Fig. 2(a, b), which shows layer separation from MAX phase Ti_3AlC_2 due to successful etching of Al. The ammonium ions intercalated during etching by NH_4HF_2 ruptured the stacked layers and resulted in delaminated $Ti_3C_2T_x$ layers. As a result, the availability of surface-active sites increases, which is helpful for further composite formation and electrochemical performance. EDS analysis (Fig. S1) further revealed very low Al weight % in the MXene, indicating the removal of Al. The porous sheet-like morphology of S-CN is shown in Fig. 2(c) (high magnification) and Fig. S1(a) (low magnification). Elemental mapping of S-CN [Fig. S1(b-e)] revealed the presence of sulfur within the carbon nitride sheets (C and N), and this trace amount of sulfur originated from the starting material thiourea. Fig. 2(d) and Fig. S2b depict homogeneous mixing of two 2D sheet-like materials, $Ti_3C_2T_x$ and S-CN, resulting in the formation of a uniform heterostructure. Similar uniform mixing of two-layered materials is visible in the FESEM images of MCN-2:1 [Fig. S2(a)] and MCN-8:1 Fig. S2(c). Furthermore, elemental mapping of MCN-4:1 [Fig. S2(d-j)] ensures the homogeneous mixing of C, N, and S (from S-CN) with MXene (Ti, C, O, and F) nanosheets. A comparison of the crystal structures of S-CN, MXene, and three binary composites, MCN-2:1, MCN-4:1, and MCN-8:1, was performed via XRD analysis, as shown in Fig. 2(e). The XRD spectrum of S-CN exhibited a strong peak at $2\theta = 27.3°$, corresponding to the (002) plane coming from the interlayer stacking of conjugated aromatic systems, and a weak peak at $2\theta = 13.2°$, attributed to the (100) plane coming from in-plane stacking of tri-s-triazine units [32]. The XRD spectrum of $Ti_3C_2T_x$ exhibited characteristic diffraction peaks at $2\theta = 7.4°$, 19.5°, 28.2°, 35.7°, 40.9°, and 61° attributed to the (002), (004), (006), (008), (0010), and (110) planes, respectively[33]. The XRD patterns of the binary MCN composites exhibit characteristic peaks of both MXene and S-CN according to their concentration, with slight shifts, indicating successful composite formation. For example, the (002) plane of pure MXene, which arises at 7.4°, shifted to approximately 7° for MCN composites [Fig. 2(f)]. Specifically, after incorporation of S-CN into MXene, the c-lattice parameter and *d*-spacing increased by 1.36 and 0.68 Å, respectively, indicating an increase in the interlayer spacing due to the intercalation of S-CN sheets between MXene layers. Interestingly, the zoomed XRD spectra in the low-2θ region [Fig. 2(f)] shows that the

(008) plane of the MXene and (002) plane of S-CN merged and resulted in one broad peak for MCN-4:1, indicating better interaction between the two components than the other two binary composites due to heterostructure formation.

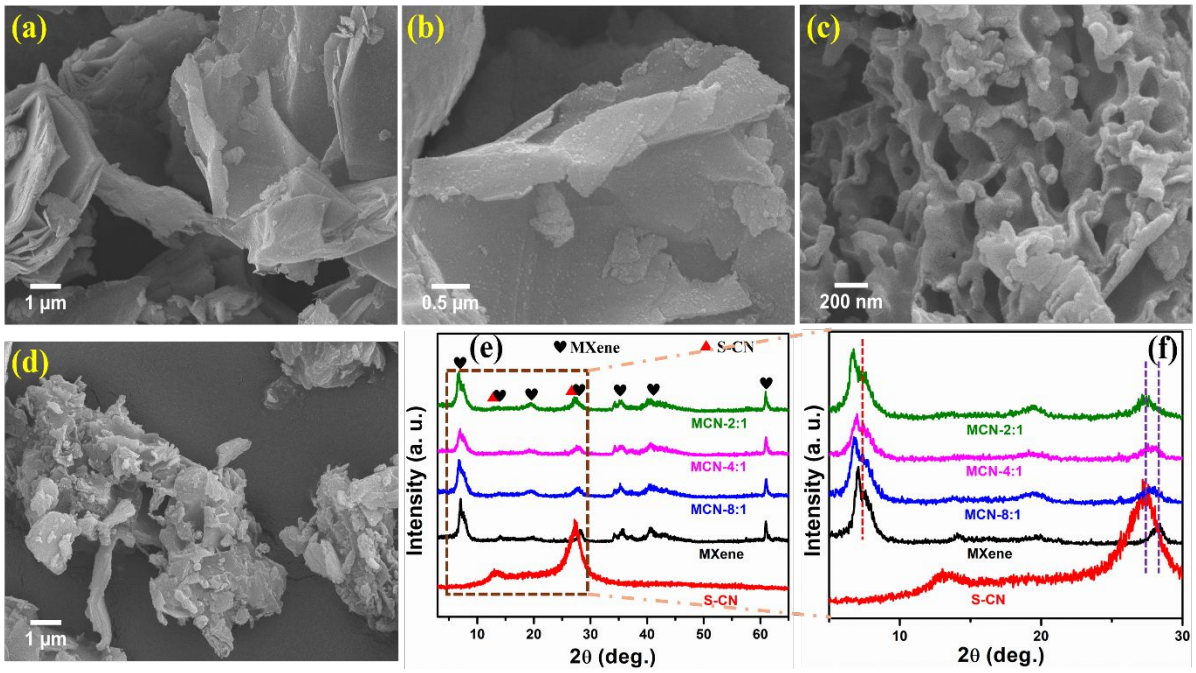

Fig 2. FESEM images of (a, b) MXene, (c) S-CN, and (d) MCN-4:1 and (e, f) XRD patterns of S-CN, MXene, MCN-8:1, MCN-4:1, and MCN-2:1.

Three-electrode electrochemical analysis in 1 M KOH was performed to determine the optimum binary composite within a voltage window of 0.0 to 0.5 V. Fig. S3(a, b) shows the electrochemical performance comparison of S-CN, MXene, MCN-2:1, MCN-4:1, and MCN-8:1 with cyclic voltammetry (CV) curves at 50 mV s^{-1} and galvanostatic charge–discharge (GCD) curves at 1 A g^{-1}, respectively. The study revealed that among all the single components and binary composites, MCN-4:1 presented the highest CV area and maximum discharge time in the GCD analysis. The MCN-4:1 electrode exhibited a maximum specific capacitance of 438.5 F g^{-1} among the other samples, including S-CN (10.8 F g^{-1}), MXene (50.4 F g^{-1}), MCN-2:1 (102.2 F g^{-1}), and MCN-8:1 (224.9 F g^{-1}), at 1 A g^{-1}. Therefore, the three-electrode study validates the superior electrochemical efficiency of MCN-4:1 with respect to the other two binary composites because of the better interaction between two individual components, which is also indicated by the XRD analysis. Thus, MCN-4:1 was further utilized to prepare ternary composites with Ce and Er selenides.

2.2. Optimization of the MCN/CESe ternary composites

The surface morphology of the MXene/S-doped graphitic carbon nitride/cerium-erbium-selenide (MCN/CESe) ternary composites was investigated via FESEM analysis, as shown in

Fig. 3(a-f). Two different morphologies of Ce and Er selenides, including particles such as Ce_2Se_3 and rods such as Er_2Se_3, are visible in the FESEM image [Fig. S2(k)]. FESEM images of MCN/CESe-3:1 [Fig. 3(a, b)] depicts a thicker coating of Ce_2Se_3 and Er_2Se_3 with an agglomerated morphology over MCN-4:1 nanosheets, indicating a higher concentration of CESe. Due to the higher concentration of CESe compared to MCN-4:1 matrix the distinct morphologies of Ce_2Se_3 and Er_2Se_3 are not clear. Uniform growth with homogeneous coatings of particles such as Ce_2Se_3 and rods such as Er_2Se_3 over the MCN-4:1 matrix as well as intercalation observed for the MCN/CESe-5:1 nanohybrid [Fig. 3(c, d)], indicating the optimum concentration of individual components. The FESEM image of MCN/CESe-7:1 shown in Fig. 3(e, f) shows an incomplete coating of metal selenides over the MCN-4:1 matrix, which is in line with the lower concentration of metal selenides used. Furthermore, FESEM elemental mapping of MCN/CESe-5:1 [Fig. S4(b-h)] revealed a homogenous distribution of Ce, Er, and Se (from CESe) over the MCN-4:1 (Ti, C, N, and S) nanosheets, indicating the formation of a ternary nanohybrid.

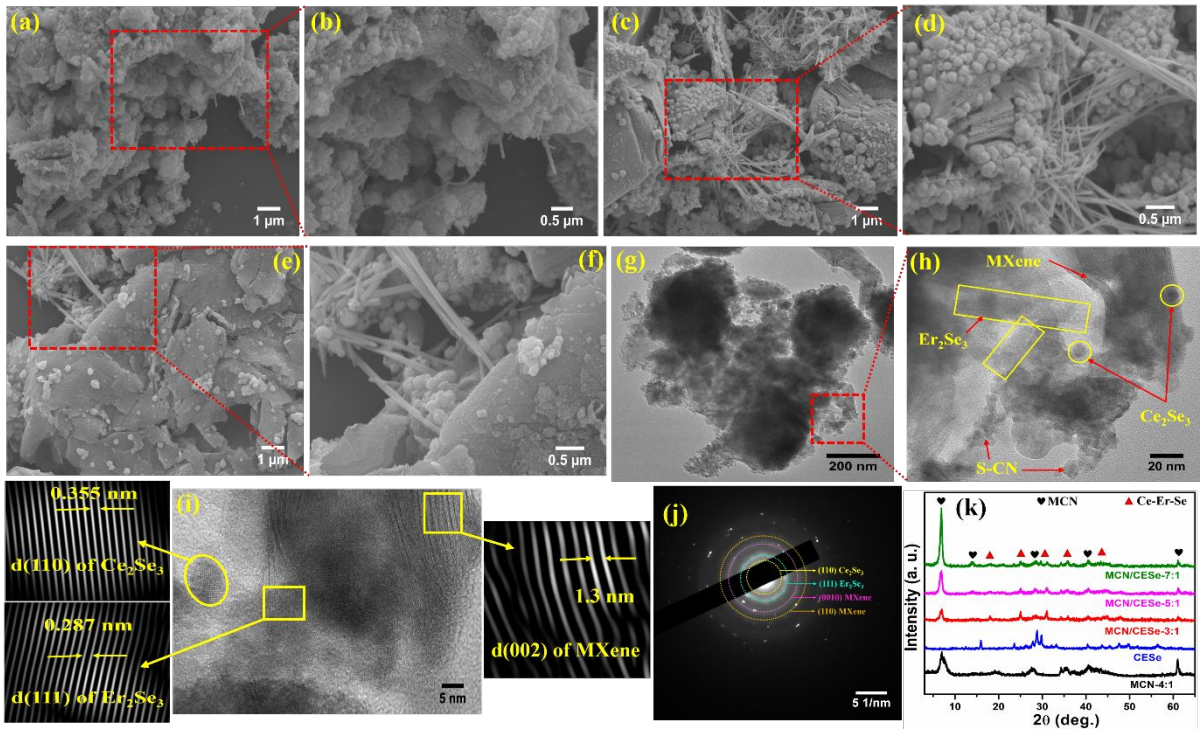

Fig. 3. FESEM images of (a, b) MCN/CESe-3:1, (c, d) MCN/CESe-5:1, (d, e) MCN/CESe-7:1; (g, h) TEM images, (i) HRTEM image with lattice fringes of MXene, Ce_2Se_3 and Er_2Se_3, (j) SAED pattern of MCN/CESe-5:1; (k) comparison of the XRD spectra of MCN-4:1, CESe, MCN/CESe-3:1, MCN/CESe-5:1, and MCN/CESe-7:1.

The XRD patterns of MCN-4:1, CESe, MCN/CESe-3:1, MCN/CESe-5:1, and MCN/CESe-7:1 are shown in Fig. 3(k). The XRD spectrum of CESe shows characteristic peaks at 2θ = 16°, 28.7°, 33°, 40.6°, 49.7°, and 56.5° correspond to the (202), (220), (311), (222), and (400) planes of Er_2Se_3[34, 35,] and the characteristic peaks at 2θ = 23.7°, 26.4°, 29.9°, 43.6°, and 47.8° correspond to the (110), (111), (012), (312), and (121) planes of Ce_2Se_3[36]. The MCN/CESe composites exhibit characteristic XRD peaks of both Ce_2Se_3 and Er_2Se_3 with little shifting, indicating interactions due to composite formation. Additionally, the characteristic peaks at 2θ = 6.7°, 14°, 28.5°, 40.5° and 61.2° exhibited by the MCN/CESe composites are associated with the planes of MCN-4:1, which are slightly shifted and broadened compared with those of the pure MCN-4:1 composite, indicating intercalation and interaction between CESe and MCN-4:1. Interestingly, the characteristic (002) plane of the MXene shifted from 7° for MCN-4:1 to 6.7° for the MCN/CESe composites, indicating the intercalation of CESe inside the MXene layers, which further increased the number of surface active sites, leading to increased electrochemical efficiency.

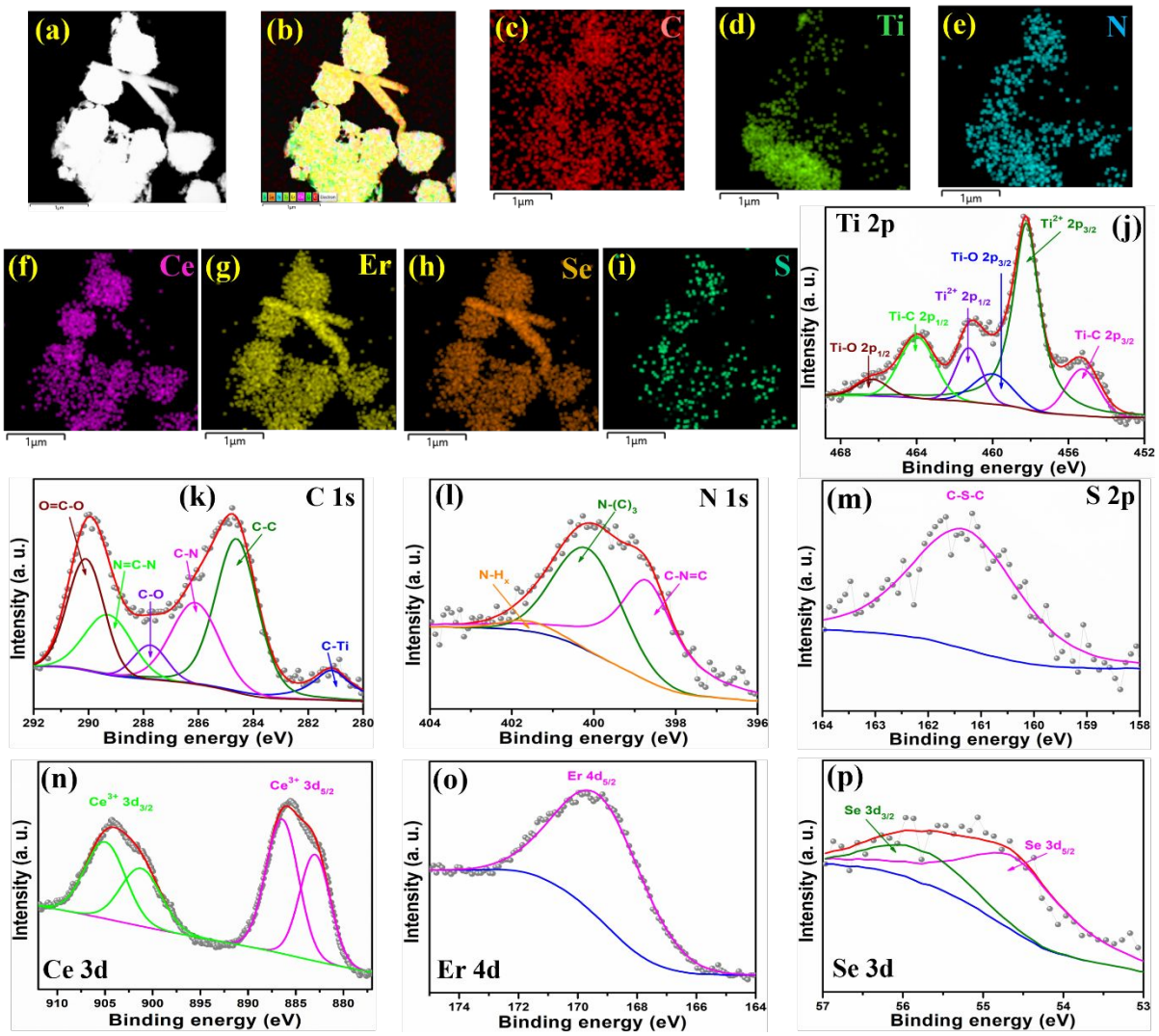

Fig. 4. (a) ADF-STEM image, (b) TEM overlay map, (c-i) elemental mapping of C, Ti, N, Ce, Er, Se, and S, respectively, of MCN/CESe-5:1; deconvoluted XPS spectra of (j) Ti 2p, (k) C 1s, (l) N 1s, (m) S 2p, (n) Ce 3d, (o) Er 4d, and (p) Se 3d of MCN/CESe-5:1.

The cross-section of MCN/CESe-5:1 was studied via TEM analysis, as shown in Fig. 3(g, h). The uniform distribution of Ce_2Se_3 particles and rod-like Er_2Se_3 over the MXene and S-CN heterostructure is clearly visible from the high-magnification TEM image shown in Fig. 3(h). The HRTEM fringes shown in Fig. 3i reveal the presence of heterojunctions between the metal selenides and the 2D sheets, which allows facile pathways for electron transfer, leading to enhanced electrochemical performance. The calculated d-spacings are 0.355, 0.287, and 1.3 nm, which correspond to the (110) plane of Ce_2Se_3, (111) plane of Er_2Se_3, and (002) plane of $Ti_3C_2T_x$, respectively. The selected area electron diffraction (SAED) pattern indicates rings consisting of multiple bright spots, indicating the polycrystalline nature of the nanohybrid. The rings obtained from the SAED pattern are indexed with characteristic XRD planes, including the (110) plane of Ce_2Se_3, the (111) plane of Er_2Se_3, and the (0010) and (110) planes of $Ti_3C_2T_x$.

The TEM elemental mapping [Fig. 4(c-i)] clearly shows that the rod-like morphology is made up of Er_2Se_3 and that the particle-like morphology arises from Ce_2Se_3 over MCN-4:1 (Ti, C, N, and S). Additionally, the homogeneous distribution of each element confirms good interaction among the individual components of MCN/CESe-5:1.

XPS analysis was performed to evaluate the valence state and bonding nature of different components in MCN/CESe-5:1. Fig. S3(c) shows a full surface survey scan of MCN/CESe-5:1, which confirms the presence of C, Ti, N, O, F, Ce, Er, Se, and S. The absence of Al in the survey scan indicates the successful etching of $Ti_3C_2T_x$ from Ti_3AlC_2. The high-resolution XPS spectra of Ti 2p shown in Fig. 4(j) exhibit six characteristic peaks at 455.3, 458.2, 460.03, 461.3, 463.96, and 466.4 eV, which are attributed to Ti−C $2p_{3/2}$, Ti^{2+} $2p_{3/2}$, Ti−O $2p_{3/2}$, Ti^{2+} $2p_{1/2}$, Ti−C $2p_{1/2}$, and Ti−O $2p_{1/2}$, respectively[37]. Here, Ti−O bonds represent surface functional groups of $Ti_3C_2T_x$. The deconvoluted C 1s spectrum shown in Fig. 4(k) depicts peaks with binding energies of 281.2, 284.65, 286.15, 287.77, 289.3, and 290.1 eV, which correspond to C−Ti, C−C, C− N, C−O, N=C−N, and O=C−O bonds, respectively[7, 38]. Fig. 4(l) shows the high-resolution N 1s XPS spectrum, which depicts characteristic peaks at 398.76, 400.24, and 401.63 eV corresponding to C−N=C, $N-(C)_3$, and NH_x bonds, respectively[39]. There is also a small peak of S 2p [Fig. 4(m)] at a binding energy of 161.4 eV corresponding to C−S−C bonds, which confirms the presence of sulfur in S-CN [38]. Fig. 4(n) shows the high-resolution XPS spectrum of Ce 3d, which depicts two Ce^{3+} doublets due to the spin-orbit coupling of Ce^{3+} $3d_{5/2}$ (883.04 and 886.48 eV) and Ce^{3+} $3d_{3/2}$ (901.3 and 905.08 eV). The spin-orbit splitting was around 18.26 eV and the intensity ratio of I $3d_{5/2}$/I $3d_{3/2}$ was fixed to 1.1[40]. For the high-resolution Er 4d XRS spectrum [Fig. 4(o)], the characteristic peak at 169.7 eV corresponds to Er^{3+} $4d_{5/2,}$ which confirms the presence of Er(III) in erbium selenide[41]. The deconvoluted XPS spectrum of Se 3d [Fig. 4(p)] shows two overlapping peaks at 54.68 and 55.87 eV, which are attributed to the Se $3d_{5/2}$ and Se $3d_{3/2}$ states, respectively, with a spin-orbit splitting of 1.19 eV, indicating a Se^{2-} valence state[36]. Therefore, an XPS study revealed S-doping in graphitic carbon nitride and the presence of Ce^{3+} and $Er^{3+,}$ confirming the formation of Ce_2Se_3 and Er_2Se_3. Thus, the formation of MCN/CESe-5:1 is evidenced by XPS analysis as well as the interactions among different components.

2.3. Supercapacitor performance

The supercapacitor performance of the synthesized samples was first optimized by a three-electrode system in 1 M KOH within a potential window of 0 to 0.5 V. Fig. 5(a) shows a comparison of the CV profiles of MCN-4:1, MCN/CESe-3:1, MCN/CESe-5:1, and

MCN/CESe-7:1 at 50 mV s^{-1}. The CV profile indicates an electrochemical double layer-type charge storage mechanism, as there is no prominent redox peak. Among the synthesized samples, the largest CV area and highest current response are exhibited by MCN/CESe-5:1 because of the synergistic mixing of $Ti_3C_2T_x$, S-CN, and CESe. The incorporation of CESe in the binary MCN-4:1 composite enhances the electrochemical performance in terms of the CV area and current response. This phenomenon is also supported by the measured conductivity of the samples, as the highest conductivity of 1247 S m^{-1} is obtained for MCN/CESe-5:1, followed by MCN-4:1 (66 S m^{-1}) and $Ti_3C_2T_x$ (953 S m^{-1}). The layered heterostructure of MCN-4:1, as observed via FESEM analysis, facilitates K^+ ion intercalation by providing more electrolyte access and producing fast electron transfer through the MCN-4:1 layer. The typical cation intercalation–deintercalation process on the surface as well as in the bulk of the $Ti_3C_2T_x$ layers can be depicted by the following Eq. (1, 2)[42]:

$$Ti_3C_2T_x + xK^+ + xe^- \leftrightarrow K_xTi_3C_2T_x \quad (1)$$

$$Ti_3C_2 + xK^+ + xe^- \leftrightarrow K_xTi_3C_2 \quad (2)$$

On the other hand, CESe nanoparticles provide high contact with the electrolyte, which increases the number of ionic interactions. Fig. 5(b) shows a comparison of the GCD profiles of the synthesized materials at 1 A $g^{-1,}$ and among them, MCN/CESe-5:1 has the longest discharge time. The highest specific capacitance (calculated via Eq. S1) of 973 F g^{-1} is obtained for MCN/CESe-5:1 compared with MCN/CESe-3:1 (680 F g^{-1}), MCN/CESe-7:1 (773 F g^{-1}) and MCN-4:1 (438.5 F g^{-1}). The superior specific capacitance of the MCN/CESe ternary composite to that of the binary MCN-4:1 composite is attributed to the significant contribution of CESe, which facilitates electron transfer within the electrode system.

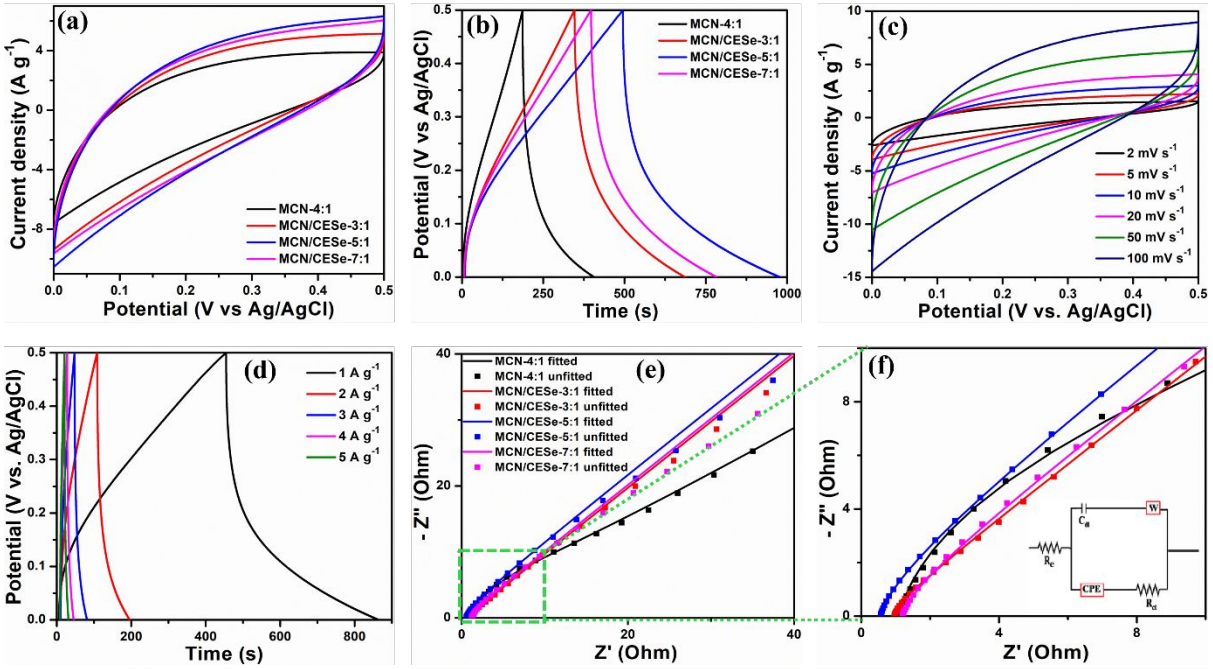

Fig. 5. (a) CV at 50 mV s^{-1} and (b) GCD at 1 A g^{-1} comparison of MCN-4:1, MCN/CESe-3:1, MCN/CESe-5:1, and MCN/CESe-7:1, (c) CV at different scan rates, and (d) GCD at different current densities of MCN/CESe-5:1. (e, f) Nyquist impedance plot of synthesized materials; the inset of (f) shows the fitting circuit.

An electrochemical impedance study was carried out to determine the resistance generated at the electrode–electrolyte interface. Fig. 5(e, f) shows a comparison of the Nyquist impedance plots of the synthesized electrodes fitted with the equivalent circuit shown in the inset of Fig. 5(f). The fitted values of the Nyquist impedance plot are summarized in Table S2. The absence of semicircle in the impedance plot indicates a low interfacial charge transfer resistance due to the rapid diffusion of ions around the electrode/electrolyte interface[43, 44]. The equivalent series resistance (R_{ESR}) describes the interfacial resistance of the electrode and the ohmic resistance of the electrolyte. The smallest R_{ESR} value for MCN/CESe-5:1 among the other synthesized composites indicates that the minimum interfacial resistance for MCN/CESe-5:1. This results in the most facile charge transfer, indicating its optimum electrochemical performance. Fig. 5(c) shows the CV curves of MCN/CESe-5:1 with different scan rates. The CV curve area and current response increase with increasing scan rate, which is a typical characteristic of supercapacitor electrodes. The corresponding GCD profiles of MCN/CESe-5:1 at different current densities represented in Fig. 5(d) follow a similar tendency to that of CV. The higher discharge time of MCN/CESe-5:1 agrees with better electrode–electrolyte interactions as well as the highest conductivity, leading to enhanced charge storage.

Therefore, a three-electrode study confirmed the optimum electrochemical performance of the MCN/CESe-5:1 nanocomposite. Therefore, the practical applicability of the MCN/CESe-5:1 nanohybrid was further tested by assembling an all-solid-state asymmetric supercapacitor (ASSASC) device within a voltage range of 0.0–1.1 V. A slurry of electroactive material was prepared following a similar three-electrode method and was coated on a piece of carbon cloth with dimensions of 2 cm × 2 cm. The mixture was then dried at 60 °C for 12 h under vacuum and used as an active electrode. Fig. S5(a-c) shows digital photographs of the bare current collectors (carbon cloth), electroactive material-coated current collectors, and assembled ASSASC device, respectively. The MCN/CESe-5:1 nanocomposite was used as the positive electrode, and MXene was used as the negative electrode. Fig. S3(d) shows a comparison of the electrochemical performance of MXenes in the negative voltage range (0.0 to −0.5 V) with that of MCN/CESe-5:1 in the positive voltage range (0.0–0.5 V) at 50 mV s^{-1} in a three-electrode setup in 1 M KOH. A high CV area for the MXene in the negative potential window is observed, which indicates its efficiency as a negative electrode. The active mass loading for the fabrication of the ASSASC device was 3.5 mg. A PVA–KOH polymer gel (synthesis method in S1) was used as both the electrolyte and separator. The PVA-KOH gel was painted over both active electrodes and dried to fabricate the ASSASC device. Fig. 6(a) shows different components of the assembled ASSASC device.

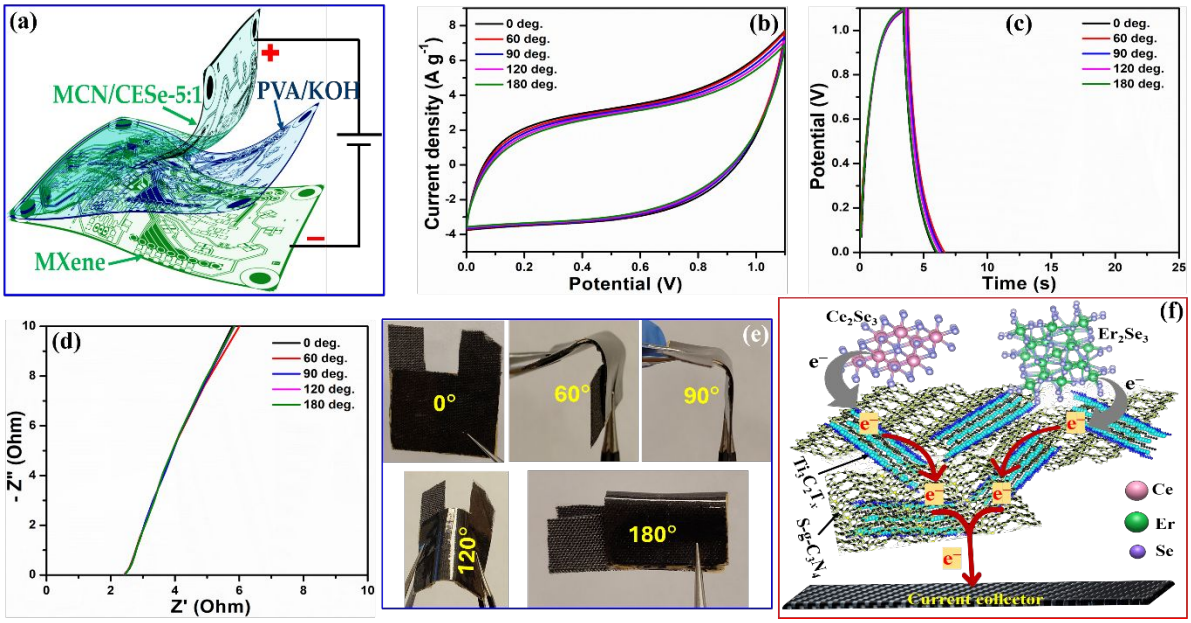

Fig. 6. (a) Schematic illustration of the assembled ASSASC device, (b) CV, (c) GCD, and (d) Nyquist plots of the ASSASC at different bending states, (e) digital photograph of the assembled ASSASC at different bending angles, and (f) schematic illustration of the probable electron transfer pathway during charging.

Fig. 6(b-d) shows the CV curves at 50 mV s^{-1}, GCD curves at 4 A g^{-1}, and Nyquist plots, respectively, keeping the device at different bending angles, including 0, 60, 90, 120, and 180°, as shown in Fig. 6(e). Under different bending states, there is no obvious change in the current response or CV area for the CV profiles, and the discharge time for the GCD is the same. Additionally, the Nyquist plots for the device overlap under various bending states. A long-term mechanical stability under repeated bending cycles was also performed to evaluate the flexibility and durability of the ASSASC device. The CV profiles and capacitance corresponding to each CV profile after different number of bending test cycles are presented in Fig. 7(a, b). It is observed that there is no sharp drop of capacitance after multiple bending test cycles and the capacitance loss was only 9 % after 200 cycles of bending test which may be due to the aging or environmental influence. Additionally, the Nyquist plots and equivalent series resistance values corresponding to each Nyquist plot after continuous bending test cycles are presented in Fig. 7(c, d). The resistance increment after repeated bending cycles was 1.1 % which is almost negligible. These results confirm the good flexibility of the assembled ASSASC device.

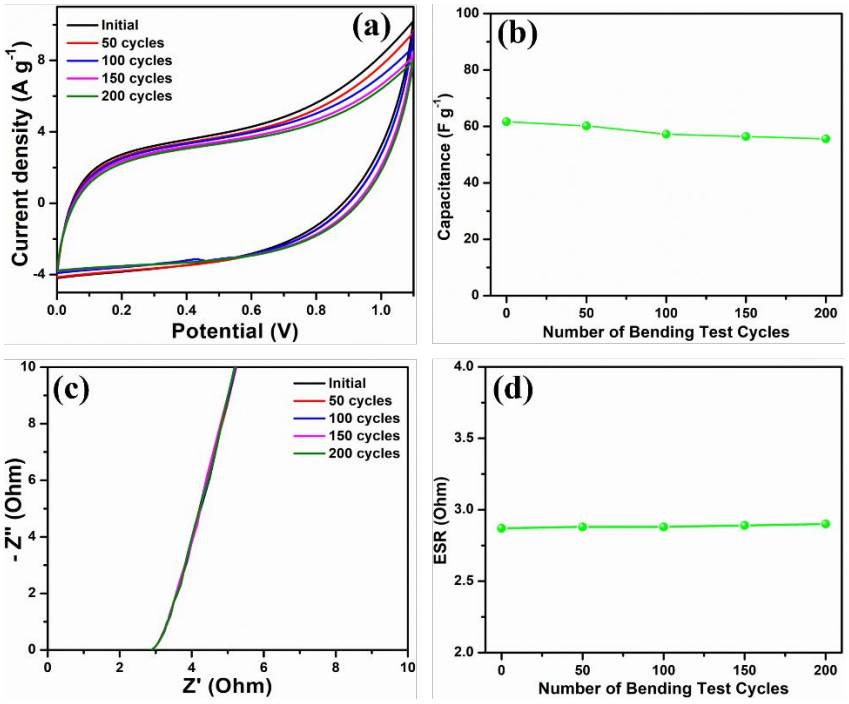

Fig. 7. After continuous bending test cycles (a) CV profiles at 50 mV s^{-1}, (b) capacitance corresponding to each CV profile, (c) Nyquist plots, and (d) equivalent series resistance (ESR) corresponding to each Nyquist plot.

Fig. S6(a) shows the CV profiles of the ASSASC device at different scan rates, which depict electrochemical double layer-type charge storage in the system, as no obvious redox peaks are visible. A similar result was obtained from the GCD analysis at varying current densities, as shown in Fig. S6(b). The specific capacitance of the device was calculated via Eq. S2. The energy density and power density of the device were calculated via Equations S3 and S4, respectively. The calculated specific capacitance, energy density, and power density of the ASSASC device are 60 F g^{-1}, 10.1 Wh kg^{-1}, and 2203.6 W kg^{-1}, respectively, at 2 A g^{-1}. Interestingly, the specific capacitance and energy density of this assembled device are much superior to those of previously reported $Ti_3C_2T_x$-based supercapacitor devices (Table S2). The ASSASC device also has the highest power density among all the devices. Furthermore, the calculated volumetric energy density of the ASSASC device was 0.9 mWh $cm^{-3,}$ which appears to be good for real-time application. Hence, the fabricated device is one of the best for practical applications in the current scenario. Fig 6(f) schematically depicts a probable electron transfer mechanism while charging occurs.

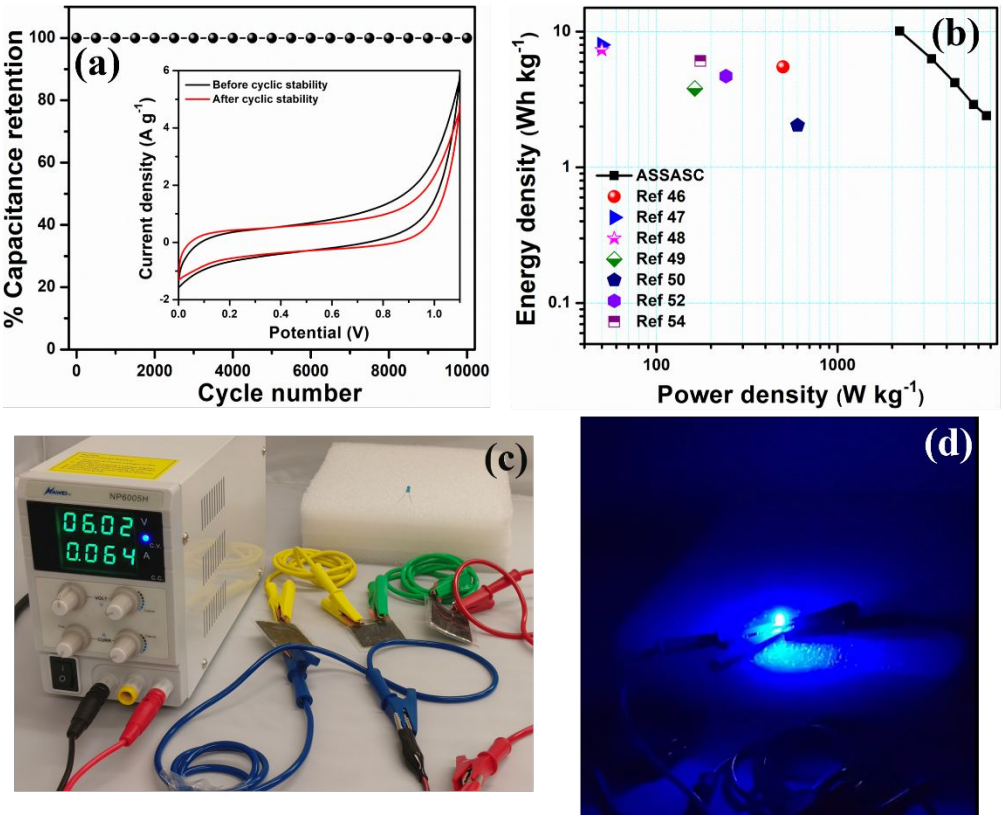

Fig 8. (a) Cyclic stability study of the ASSASC device, where the inset shows the CV profile before and after the stability study at 50 mV s^{-1}, (b) Ragone plot; photograph of (c) charging setup of three flexible ASSASC devices, and (d) a light blue LED.

The flexible ASSASC device showed a superb cycling life with ~100% specific capacitance retention for up to 10,000 charging–discharging cycles [Fig. 8(a)]. The CV profiles before and after the cyclic stability study at 50 mV s^{-1} are shown in the inset of Fig. 8(a). The almost identical CV areas before and after the stability study indicate the excellent stability of the electrode material after continuous charge–discharge cycles. The FESEM image [Fig. S5(d)] of MCN/CESe-5:1 after the stability study shows a stable morphology of particle-like Ce_2Se_3 and rod-like Er_2Se_3 decorated over the MCN layers, which is in accordance with the cycling stability results. Fig. 8(b) shows a Ragone plot, which shows that the energy density and power density of the assembled ASSASC device are much greater than that of previously reported $Ti_3C_2T_x$-based devices (+//-), such as $Ti_3C_2T_x$/N-doped carbon foam//$Ti_3C_2T_x$/N-doped carbon foam (8.75 Wh kg^{-1} and 1871 W kg^{-1})[45], $Ti_3C_2T_x$//activated carbon (5.5 Wh kg^{-1} and 500 W kg^{-1})[46], reduced graphene oxide (rGO)//$Ti_3C_2T_x$ (8 Wh kg^{-1} and 50 W kg^{-1})[47], MXene/carbon nanotube//MXene (7.34 Wh kg^{-1} and 50 W kg^{-1})[48], MXene/rGO//MXene/rGO (3.81 Wh kg^{-1} and 163 W kg^{-1})[49], MXene/metal porphyrin frameworks//MXene/metal porphyrin frameworks (2.04 Wh kg^{-1} and 601.5 W kg^{-1})[50], N-$Ti_3C_2T_x$//N-$Ti_3C_2T_x$ (9.57 Wh kg^{-1} and 250 W kg^{-1})[51], $Ti_3C_2T_x$//$Ti_3C_2T_x$ (4.7 Wh kg^{-1} and 242 W kg^{-1})[52], MXene/non-peripheral octamethyl-substituted copper (II) phthalocyanine (N-$CuMe_2Pc$)//MXene/N-$CuMe_2Pc$ (8.84 Wh kg^{-1} and 112.3 W kg^{-1})[53], and freeze-dried MXene//freeze-dried MXene (6.1 Wh kg^{-1} and 175 W kg^{-1})[54]. Interestingly, MCN/CESe-5:1 exhibited the highest specific capacitance in three electrode study among the above mentioned $Ti_3C_2T_x$-based electrodes indicating a benchmark supercapacitor performance. The real-time application of the optimum electrode for lighting LEDs is further studied. Fig. 8(c) shows the charging setup of three flexible ASSASC devices with series connections. The ASSASC devices were able to illuminate a blue LED (3.2 V), as shown in Fig. 8(d). Interestingly, bending in different states does not affect the practical applicability of the devices, as there is no change in the brightness of the LEDs under bending conditions, as shown in Fig. S6(c, d). This study indicates the excellent flexibility of the assembled devices for real-time application, indicating their potential for future portable and wearable electronic devices. Overall, MCN/CESe-5:1 exhibited excellent performance toward flexible supercapacitors with good specific capacitance, energy density, and power density due to the synergistic effect of the conducting matrix of MCN-4:1 and the ordered growth of Ce_2Se_3 and Er_2Se_3 over the 2D/2D heterostructure of MCN-4:1, enabling facile electron transfer within the electrode.

2.4. Oxygen evolution reaction performance

The electrocatalytic performance of blank glassy carbon, MXene, MCN-4:1, MCN/CESe-3:1, MCN/CESe-5:1, MCN/CESe-7:1 and commercial RuO_2 (for comparison) toward the OER was evaluated in 1 M KOH. Fig. 9(a) shows the linear sweep voltammetry (LSV) analysis of the electrodes within 1.2–2.0 V vs. RHE at 20 mV s^{-1}. Among the synthesized samples, MCN/CESe-5:1 has the highest current density of 139 mA cm^{-2} at 2.0 mV, with the lowest onset potential of ~1.48 V vs. RHE, and this result is the closest to that of the commercial RuO_2 electrocatalyst. On the other hand, the blank glassy carbon electrode does not show any electrocatalytic performance. The LSV profiles of MCN/CESe-5:1 at different scan rates are depicted in Fig. S7(a), and the LSV curves follow the typical trend of increasing current density with increasing scan rates. A comparison of the potentials (vs. RHE) required for the electrodes to obtain a current density of 10 mA cm^{-2}, which is noted as the required voltage (overpotential) for solar water splitting with 10% efficiency, is shown in Fig. 9(b)[7]. The lowest overpotential of 280 mV at 10 mA cm^{-2} is acquired for MCN/CESe-5:1 compared with the other synthesized electrodes, including MXene (550 mV), MCN-4:1 (370 mV), MCN/CESe-3:1 (300 mV), and MCN/CESe-7:1 (330 mV). Interestingly, the overpotential of the optimum electrocatalyst MCN/CESe-5:1 is comparable to that of commercial RuO_2 (250 mV). Table S3 summarizes the comparison of the overpotential values of previously reported MXene-based electrocatalysts with our optimum electrode, and it is observed that MCN/CESe-5:1 results in the lowest overpotential, indicating its efficient electrocatalytic performance toward the OER.

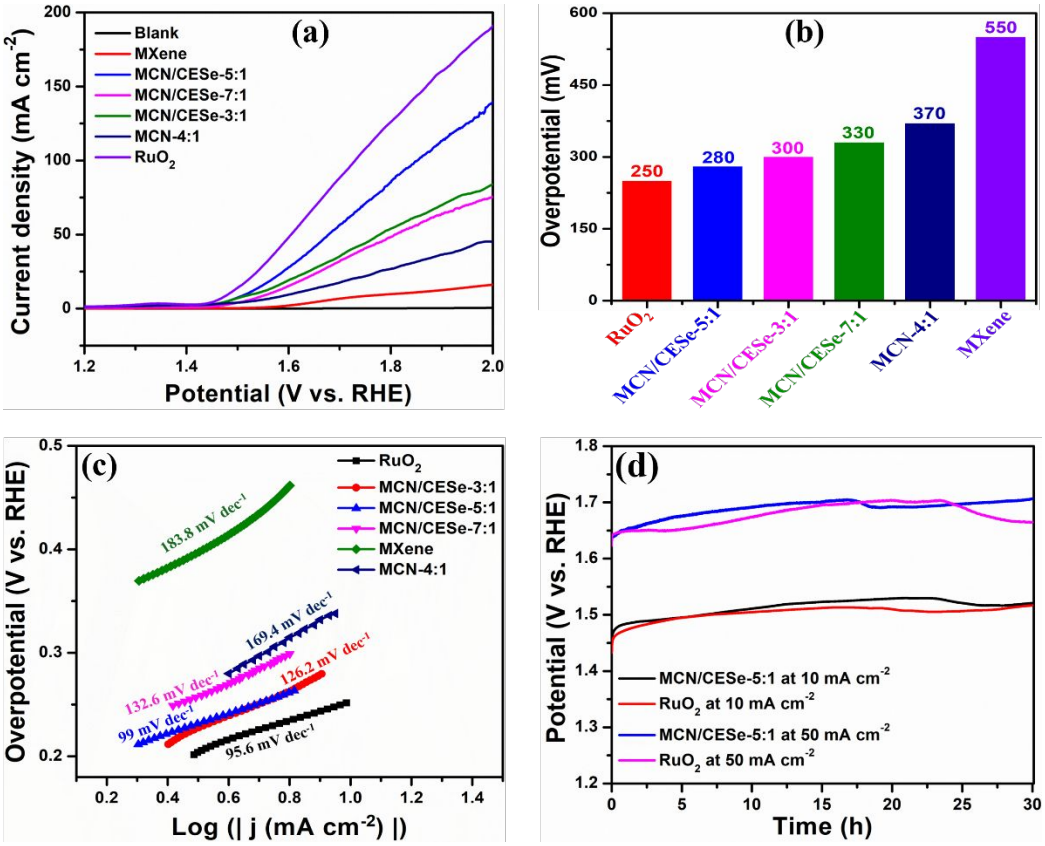

Fig. 9. (a) LSV curves at 20 mV s^{-1}, (b) overpotential at 10 mA cm^{-2}, (c) Tafel plots, and (d) chronopotentiometric stability comparison of MCN/CESe-5:1 and RuO_2 at 10 and 50 mA cm^{-2}.

The kinetic pathway of the synthesized electrocatalysts was investigated via Tafel plots [Fig. 9(c)], which were obtained by plotting the log of the current density against the overpotential and then fitted with the Tafel equation (Eq. S10). The lowest Tafel slope of 99 mV dec^{-1} is obtained for MCN/CESe-5:1 among the synthesized electrocatalysts, such as MCN/CESe-3:1 (126.2 mV dec^{-1}), MCN/CESe-7:1 (132.6 mV dec^{-1}), MCN-4:1 (169.4 mV dec^{-1}), and MXene (183.8 mV dec^{-1}). On the other hand, the Tafel slope of commercial RuO_2 (95.6 mV dec^{-1}) is also comparable with that of our synthesized optimum electrocatalyst MCN/CESe-5:1. Interestingly, the Tafel slope of MCN/CESe-5:1 is comparable to that of the previously reported MXene-based electrocatalysts summarized in Table S3. Additionally, the exchange current density, which reflects the rate of the reaction at equilibrium (η=0), was calculated from the Tafel plots. MCN/CESe-5:1 has the largest exchange current density of 1.84 mA $cm^{-2,}$ indicating the fastest reaction rate at equilibrium among all the prepared electrocatalysts, including MCN/CESe-3:1 (1.32 mA cm^{-2}) and MCN/CESe-7:1 (1.44 mA cm^{-2}). MCN-4:1 (1.05 mA cm^{-2}), and MXene (0.88 mA cm^{-2}).

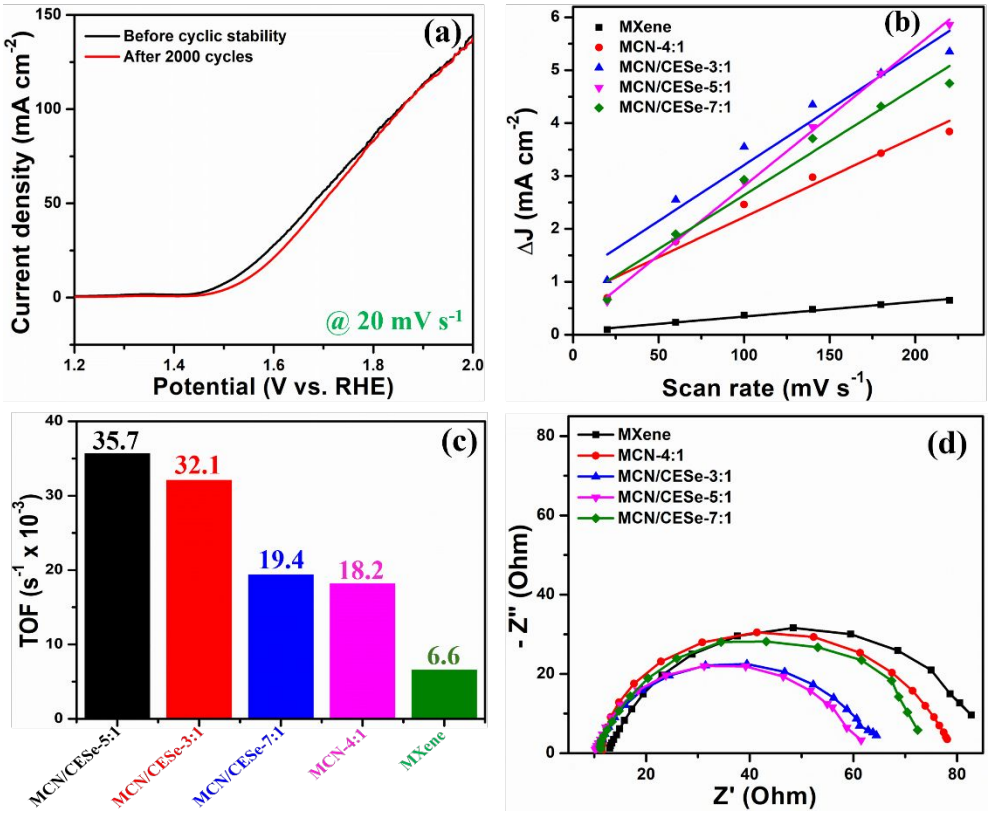

Fig. 10. (a) LSV profiles of MCN/CESe-5:1, (b) linear fitting plots of the current density difference against the scan rate, (c) bar plots comparing the TOF, and (d) EIS plots of the synthesized electrocatalysts.

The durability of an electrocatalyst toward the OER is an important parameter for its application in future energy technology. The choronopotentiometric stability of the MCN/CESe-5:1 electrocatalyst was compared with commercial RuO_2 electrocatalyst at 10 and 50 mA cm^{-2} current densities for 30 h [Fig. 9(d)]. The MCN/CESe-5:1 catalyst showed outstanding stability with the potential retention of 96.7% for 10 mA cm^{-2} current density and 96.1% for 50 mA cm^{-2} current density which is comparable with commercial RuO_2 catalyst (retention 96.2% for 10 mA cm^{-2} current density and 98.9% for 50 mA cm^{-2} current density). Furthermore, a comparison of the LSV profiles of MCN/CESe-5:1 before and after 2000 cycles at 20 mV s^{-1} is depicted in Fig. 10(a). The almost negligible change in the LSV profile in terms of current density and onset potential after 2000 cycles indicates the structural stability and durable electrocatalytic performance of MCN/CESe-5:1 toward the OER. Furthermore, the electrochemical double layer capacitance (C_{dl}) of the solid–liquid interface and electrochemically active surface area (ECSA) of the synthesized materials were evaluated following the methods described in the supporting information S2. The linear fitting plots of the current density difference against the scan rate of the synthesized electrocatalysts are shown in Fig. 10(b). The calculated C_{dl} and ECSA values of the prepared electrocatalysts are

summarized in Table S4. The highest C_{dl} (26.22 mF cm^{-2}) and ECSA (655.5 cm^2) are obtained for MCN/CESe-5:1 among the synthesized electrocatalysts, which indicates the efficiency of the electrocatalytic performance toward the OER. The turnover frequency (TOF) was calculated following the process described in the supporting information S3 to quantify the intrinsic OER performance. Fig. 10(c) shows a comparison of the TOF values of the prepared materials, and MCN/CESe-5:1 delivered the highest TOF value (35.7×10^{-3} s^{-1}) among them. This result indicates that the incorporation of the multimetal centers Ce and Er within MCN-4:1 effectively increases the intrinsic OER efficiency compared with the individual components. In addition, Fig. 10(d) shows the EIS curves of the synthesized materials, and among all the synthesized nanomaterials, MCN/CESe-5:1 has a lower solution and contact resistance, which signifies the superior electrocatalytic performance of MCN/CESe-5:1.

3. Conclusion

This study reports the successful hydrothermal fabrication of Ce_2Se_3- and Er_2Se_3-grown MCN nanohybrids and the investigation of their bifunctional efficiency toward flexible ASSASC as well as the OER. Among the fabricated nanohybrids, MCN/CESe-5:1 delivered the optimum electrochemical performance for both flexible supercapacitors and the OER. The assembled flexible ASSASC device (MCN/CESe-5:1//$Ti_3C_2T_x$) exhibited a high specific capacitance of 60 F g^{-1} and an energy density of 10.1 Wh kg^{-1} (volumetric energy density: 0.9 mW h cm^{-3}) at 2 A g^{-1} with 100% capacitance retention after 10,000 charge–discharge cycles. Additionally, the assembled device depicted good flexibility toward real-time applications, indicating potential applications toward future portable and wearable devices. Furthermore, MCN/CESe-5:1 showed a low overpotential of 280 mV and a Tafel slope of 99 mV dec^{-1} with durable electrocatalytic performance. These significant outcomes highlight the potential of the MCN/CESe-5:1 nanohybrid as a versatile electrode material with a transformative impact on future energy storage and conversion applications.

Overall, the excellent electrochemical efficiency of MCN/CESe-5:1 toward flexible all-solid-state asymmetric supercapacitors as well as the OER can be attributed to the following factors.

(a) The presence of different metal centers increases the number of surface-active sites.
(b) The synergistic effect of individual components resulted in enhanced electrochemical performance, as shown by the performance comparison of the individual and composite materials.

(c) The ordered heterostructure and conducting matrix of MCN-4:1 facilitate electrode–electrolyte interactions.
(d) The presence of different interfaces provides facile electron transfer pathways.

4. Experimental Section

Materials: MAX phase (Ti_3AlC_2), erbium (III) chloride hexahydrate ($ErCl_3.6H_2O$), and polyvinylidene fluoride (PVDF) were purchased from Sigma–Aldrich, USA. Cerium(III) nitrate hexahydrate ($Ce(NO_3)_3.6H_2O$) was purchased from ACROS, USA. Thiourea, N-methyl-2-pyrrolidone (NMP, 99.5%), and carbon black were procured from Alfa Aesar, USA. Ammonium bifluoride (NH_4HF_2) was acquired from Ricca Chemical Company, USA. Se powder, polyvinyl alcohol (PVA, 98–99%, high molecular weight), ethanol (96%, v/v), and potassium hydroxide (KOH) were obtained from Thermo Fisher Scientific, USA. Cetyltrimethylammonium bromide (CTAB) was procured from MP Biomedicals, and hydrazine monohydrate ($N_2H_4.H_2O$ (>98%) was purchased from TCI, USA.

Characterization techniques: The crystal structure of the synthesized materials was studied via X-ray diffraction (XRD) analysis on a Rigaku MiniFlex 600 with Cu Kα at a wavelength of 1.5406 Å. The conductivity of the samples was measured via an Ossila P2010A2 four-point probe. Morphology and elemental mapping were investigated via field emission scanning electron microscopy (FESEM) and energy dispersive X-ray spectroscopy (EDS)-Mapping, respectively, on a JEOL JSM-IT800 Schottky instrument. The internal topography of the sample was obtained via high-resolution transmission electron microscopy (HRTEM) on a JEOL 2100PLUS instrument at 200 kV with an EDS facility. Kratos Axis Supra X-ray photoelectron spectroscopy (XPS) was used to characterize the elemental composition and bonding state of the sample. Electrochemical analysis was carried out with a BioLogic VSP-50 electrochemical workstation.

Synthesis of MXene ($Ti_3C_2T_x$): MXene ($Ti_3C_2T_x$) was prepared from its precursor MAX phase (Ti_3AlC_2) by selective aluminum etching following a previously reported strategy with slight modifications [55]. Typically, 500 mg of Ti_3AlC_2 was added slowly into a 20 ml solution of 2 M ammonium bifluoride. The mixture was then stirred constantly at 200 rpm for 36 h at 45 °C. After completion of the reaction, the solution was neutralized by washing several times with water and ethanol via centrifugation until the pH of the solution reached ~6. The final product was vacuum dried at 60 °C for 12 h.

Synthesis of S-doped graphitic carbon nitride (g-C_3N_4): S-doped g-C_3N_4 was prepared via a simple thermal polymerization method reported previously [56]. Briefly, thiourea (5 g) was added

to a covered crucible and heated at 500 °C for 2 h at a heating rate of 5 °C min^{-1}. After cooling naturally at room temperature, the sample was ground into a fine powder and labeled S-CN.

Synthesis of the MXene/S-doped graphitic carbon nitride (MCN) binary composite: For the synthesis of MCN binary composites, $Ti_3C_2T_x$ and S-CN were mixed at certain ratios in 50 ml of DI water and ethanol (1:1 v/v). The solution was shaken with Ar purging in an orbital shaker for 12 h at 160 rpm to obtain a homogeneous mixture. After that, the product was separated by centrifugation and dried under vacuum at 60 °C for 12 h to obtain the MCN composites. The MXene and S-CN ratios (w/w) were varied by 2:1, 4:1, and 8:1, and the products were designated MCN-2:1, MCN-4:1, and MCN-8:1, respectively. The ratios of these three binary composites were further optimized via three-electrode electrochemical analysis.

Synthesis of the MXene/S-doped graphitic carbon nitride/cerium-erbium-selenide (MCN/CESe) ternary composite: The ternary composite of MCN and cerium-erbium-selenide (MCN/CESe) was prepared via a facile hydrothermal method following a previously reported procedure [7]. Briefly, MCN was added to a 1:1 (v/v) mixture (60 ml) of DI water and ethanol under constant stirring. After that, $Ce(NO_3)_3.6H_2O$ and $ErCl_3.6H_2O$ were added to the homogeneous MCN-4:1 dispersion, maintaining a 1:1 ratio of Ce and Er. After 1 h, 0.05 g of CTAB was added to the mixture while stirring. Separately, Se powder was added to 10 ml of N_2H_4. H_2O and stirred for 12 h. Then, the resulting Se solution was added dropwise into the MCN-4:1 and metal salt mixture. The resulting solution was poured into a stainless steel-lined Teflon autoclave and treated hydrothermally for 24 h at 180 °C. After cooling to room temperature, the product was washed with water and ethanol via centrifugation. The obtained sample MCN-CESe was then dried under vacuum at 60 °C for 12 h. The MCN-4:1 and Ce/Er ratios were 3:1, 5:1, and 7:1, and the samples were termed MCN/CESe-3:1, MCN/CESe-5:1, and MCN/CESe-7:1, respectively. Eqs. (3-5) depict the growth mechanism of $CeSe_2$ and Er_2Se_3 over the MCN matrix.

$$2Se + 5N_2H_4 \rightarrow 2Se^{2-} + N_2\uparrow + 4N_2H_5^{+} \quad (3)$$

$$Ce^{3+} + Se^{2-} \rightarrow Ce_2Se_3 \quad (4)$$

$$Er^{3+} + Se^{2-} \rightarrow Er_2Se_3 \quad (5)$$

Supporting Information

The supporting information contains (1) synthesis of the PVA/KOH gel electrolyte, (2) electrochemical measurements for supercapacitors and the OER, (3) calculation methods for C_{dl}, the ECSA, and the TOF, (4) FESEM, EDX, and elemental mapping, (5) CV and GCD profiles, (6) XPS survey scans, (7) digital pictures of the ASSASC showing flexibility, and (8)

comparison of the supercapacitor and OER performances of the optimum sample with those of previous reports.

Declaration of competing interest

The authors declare that they have no known competing financial interests.

Data availability

The data will be made available upon request.

Acknowledgments

This work was supported by DOE BES-RENEW award number DE-SC0024611.

References

1. S. De, S. Acharya, C. K. Maity and G. C. Nayak, *ACS Applied Nano Materials*, 2023, **6**, 11175-11186.
2. D. Gogoi, R. S. Karmur, M. R. Das and N. N. Ghosh, *Journal of Materials Chemistry A*, 2023, **11**, 23867-23880.
3. M. D. Ashie and B. P. Bastakoti, *Small*, 2024, **20**, 2310927.
4. R. Dahal, R. Srivastava and B. Prasad Bastakoti, *ChemistryOpen*, 2024, **14**, e202400173.
5. B. R. KC, D. Kumar and B. P. Bastakoti, *Journal of Materials Science*, 2024, 1-14.
6. S. De and B. Bastakoti, *Journal of Materials Chemistry A*, 2025, **23**, 855-888.
7. S. De, S. Roy and G. C. Nayak, *Materials Today Nano*, 2023, **22**, 100337.
8. K. R. G. Lim, A. D. Handoko, S. K. Nemani, B. Wyatt, H.-Y. Jiang, J. Tang, B. Anasori and Z. W. Seh, *ACS Nano*, 2020, **14**, 10834-10864.
9. C. Young, T. Park, J. W. Yi, J. Kim, M. S. A. Hossain, Y. V. Kaneti and Y. Yamauchi, *ChemSusChem*, 2018, **11**, 3546-3558.
10. S. M. M. Alonzo, S. De, V. Morris, D. E. Autrey, B. R. Gautam, G. Pathiraja and B. P. Bastakoti, *ACS Applied Materials Interfaces,* 2024, **16**, 64784-64796.
11. T. Zhou, C. Wu, Y. Wang, A. P. Tomsia, M. Li, E. Saiz, S. Fang, R. H. Baughman, L. Jiang and Q. Cheng, *Nature communications*, 2020, **11**, 2077.
12. Y. Wu, W. Wei, R. Yu, L. Xia, X. Hong, J. Zhu, J. Li, L. Lv, W. Chen and Y. Zhao, *Advanced Functional Materials*, 2022, **32**, 2110910.
13. R. Ma, X. Zhang, J. Zhuo, L. Cao, Y. Song, Y. Yin, X. Wang, G. Yang and F. Yi, *ACS Nano*, 2022, **16**, 9713-9727.
14. M. Zaed, J. Cherusseri, R. Saidur, K. Tan and A. Pandey, *Open Ceramics*, 2024, **19**, 100645.
15. C. Lu and X. Chen, *ACS nano*, 2021, **15**, 18777-18793.
16. H. He, Y. Chen, C. Yang, L. Yang, Q. Jiang and H. Huang, *Journal of Energy Chemistry*, 2022, **67**, 483-491.
17. M. Depijan, K. Hantanasirisakul and P. Pakawatpanurut, *ACS omega*, 2024, **9**, 22256-22264.
18. M. Mahanthappa, M. P. Bhat and A. Alshoaibi, *International Journal of Hydrogen Energy*, 2024, **84**, 641-649.
19. J. Zhu, L. Xia, W. Yang, R. Yu, W. Zhang, W. Luo, Y. Dai, W. Wei, L. Zhou and Y. Zhao, *Energy Environmental Materials*, 2022, **5**, 655-661.
20. B. R. KC, D. Kumar and B. P. Bastakoti, *Journal of Physics: Energy*, 2025, **7**, 022001.
21. S. M. M. Alonzo, M. D. Ashie, G. Pathiraja and B. P. Bastakoti, *Chemical Engineering Journal*, 2025, 159208.
22. X. Li, Y. Guo, Y. Li and R. Fu, *ACS Applied Energy Materials*, 2023, **6**, 5774-5786.
23. B. Pandit, A. Agarwal, P. Patel and B. R. Sankapal, *Nanoscale Advances*, 2021, **3**, 1057-1066.
24. S. Manzoor, F. Alharbi, A. G. Al-Sehemi, M. N. Ashiq, A. G. Abid, R. Y. Khosa, M. N. Ansari, S. Trukhanov, D. Tishkevich and A. Trukhanov, *Materials Chemistry Physics*, 2023, **301**, 127529.
25. I. L. Ikhioya, C. Udeze, F. U. Ochai-Ejeh, I. Ahmed, M. Maaza and F. I. Ezema, *Journal of the Indian Chemical Society*, 2022, **99**, 100793.
26. I. L. Ikhioya, C. O. Ugwuoke and F. U. Ochai-Ejeh, *Materials Research Innovations*, 2024, **28**, 32-39.
27. S. Fatima, M. Anwar, A. S. Almalki, A. Alhadhrami, M. F. Warsi and Z. M. El-Bahy, *Ceramics International*, 2024, 50, 29201-29212.
28. K. M. Katubi, A. Rasheed, A. Ihsan, B. Shaheen, Z. Alrowaili, M. Al-Buriahi, M. I. Din, I. Shakir and S. Munir, *Optical Materials*, 2024, **152**, 115390.
29. L. Wang, C. Wang and Q. Yuan, *Ceramics International*, 2024, **50**, 21726-21735.
30. T. Tahir, K. Chaudhary, M. F. Warsi, M. S. Saif, I. A. Alsafari, I. Shakir, P. O. Agboola, S. Haider and S. Zulfiqar, *Ceramics International*, 2022, **48**, 1969-1980.

31. T. Tahir, D. Alhashmialameer, S. Zulfiqar, A. M. Atia, M. F. Warsi, K. Chaudhary and H. M. El Refay, *Ceramics International,* 2022, **48**, 24840-24849.
32. S. Vinoth, K. Subramani, W.-J. Ong, M. Sathish and A. Pandikumar, *Journal of Colloid Interface Science*, 2021, **584**, 204-215.
33. M. Shekhirev, C. E. Shuck, A. Sarycheva and Y. Gogotsi, *Progress in Materials Science*, 2021, **120**, 100757.
34. D. Haase, H. Steinfink and E. Weiss, *Inorganic Chemistry*, 1965, **4**, 538-540.
35. C. Fang, A. Meetsma and G. Wiegers, *Journal of alloys compounds*, 1995, **218**, 224-227.
36. B. Pandit and B. R. Sankapal, *ACS Applied Nano Materials*, 2022, **5**, 3007-3017.
37. L. Yao, X. Tian, X. Cui, R. Zhao, X. Xiao and Y. Wang, *Journal of Materials Science: Materials in Electronics*, 2021, **32**, 27837-27848.
38. Y. Quan, R. Li, X. Li, R. Chen, Y. H. Ng, J. Huang, J. Hu and Y. Lai, *Small*, 2024, 2406576.
39. Q. Zeng, X. Wang, M. Jin, E. M. Akinoglu, G. Zhou and L. Shui, *Journal of Colloid Interface Science*, 2020, **578**, 788-795.
40. I. Othman, J. H. Zain, M. A. Haija and F. Banat, *Applied Catalysis B: Environmental*, 2020, **266**, 118601.
41. X. Sun, G. Sun and M. Huang, *Journal of the American Ceramic Society*, 2024, **107**, 1408-1418.
42. M. R. Lukatskaya, O. Mashtalir, C. E. Ren, Y. Dall'Agnese, P. Rozier, P. L. Taberna, M. Naguib, P. Simon, M. W. Barsoum and Y. Gogotsi, *Science*, 2013, **341**, 1502-1505.
43. M. Y. Perdana, B. A. Johan, M. Abdallah, M. E. Hossain, M. A. Aziz, T. N. Baroud and Q. A. Drmosh, *The Chemical Record*, 2024, **24**, e202400007.
44. G. Singh, Y. Kumar and S. Husain, *Journal of Energy Storage*, 2020, **31**, 101660.
45. L. Sun, G. Song, Y. Sun, Q. Fu and C. Pan, *ACS Applied Materials Interfaces*, 2020, **12**, 44777-44788.
46. T.-H. Chang, T. Zhang, H. Yang, K. Li, Y. Tian, J. Y. Lee and P.-Y. Chen, *ACS Nano*, 2018, **12**, 8048-8059.
47. A. M. Navarro-Suárez, K. L. Van Aken, T. Mathis, T. Makaryan, J. Yan, J. Carretero-González, T. Rojo and Y. Gogotsi, *Electrochimica Acta*, 2018, **259**, 752-761.
48. X. Shi, F. Guo, K. Hou, G. Guan, L. Lu, Y. Zhang, J. Xu and Y. Shang, *Energy & Fuels*, 2023, **37**, 9704-9712.
49. D. Jiang, J. Zhang, S. Qin, Z. Wang, K. A. S. Usman, D. Hegh, J. Liu, W. Lei and J. M. Razal, *ACS Nano*, 2021, **15**, 5000-5010.
50. W. Zhao, J. Peng, W. Wang, B. Jin, T. Chen, S. Liu, Q. Zhao and W. Huang, *Small*, 2019, **15**, 1901351.
51. M. Cai, X. Wei, H. Huang, F. Yuan, C. Li, S. Xu, X. Liang, W. Zhou and J. Guo, *Chemical Engineering Journal*, 2023, **458**, 141338.
52. X. Zhang, Y. Liu, S. Dong, J. Yang and X. Liu, *Journal of Alloys Compounds*, 2019, **790**, 517-523.
53. R. Ramachandran, Q. Hu, K. Rajavel, P. Zhu, C. Zhao, F. Wang and Z.-X. Xu, *Journal of Power Sources*, 2020, **471**, 228472.
54. F. Ran, T. Wang, S. Chen, Y. Liu and L. Shao, *Applied Surface Science*, 2020, **511**, 145627.
55. M. Pahlevaninezhad, R. Sadri, D. Momodu, K. Eisawi, M. Pahlevani, M. Naguib and E. P. Roberts, *Batteries Supercaps*, 2024, **7**, e202300473.
56. S. She, Y. Wang, R. Chen, F. Yi, C. Sun, J. Hu, Z. Li, G. Lu and M. Zhu, *Chemosphere*, 2021, **266**, 128929.

Data are available from the corresponding author upon reasonable request